1992

He+ 2p state lifetime by a quenching-asymmetry measurement

Gordon W. F. Drake
University of Windsor

J. Kwela

A. Van Wijngaarden

He$^+$ 2p state lifetime by a quenching-asymmetry measurement

G. W. F. Drake, J. Kwela, and A. van Wijngaarden

Department of Physics, University of Windsor, Windsor, Ontario, Canada N9B 3P4

(Received 20 December 1991)

An interference asymmetry in the angular distribution of the Ly-α quenching radiation emitted by He$^+$ ions in the metastable $2s_{1/2}$ state is measured to high precision to obtain the lifetime of the $2p_{1/2}$ state. The derived lifetime of $(0.99717 \pm 0.00075) \times 10^{-10}$ s is the most accurate available for a fundamental atomic system. A detailed discussion of systematic corrections is included. The result is in good agreement with theory, thereby confirming the theory of radiative transition probabilities to $\pm 0.075\%$, and indicating that differences between theory and experiment for the alkali metals must be due to either inadequate wave functions or experimental errors.

PACS number(s): 32.70.Fw

I. INTRODUCTION

Over the past two decades we have carried out a series of measurements [1,2] on interference effects in the electric-field-induced Ly-α quench radiation of hydrogenic ions in the metastable $2s_{1/2}$ state. High-precision measurements of fundamental quantities, in particular the $2s_{1/2}$-$2p_{1/2}$ Lamb shift [3] and $2p$ lifetime [4,5], have been obtained from studies of the angular distribution of the emitted radiation. This paper reports an improvement in our earlier $\pm 0.26\%$ measurement of the He^+2p lifetime [5] to the $\pm 0.075\%$ level of accuracy.

The method of measurement exploits an asymmetry in the quench radiation from a beam of spin-polarized He$^+(2s)$ ions that is proportional to $(\hat{\mathbf{k}} \cdot \hat{\mathbf{E}}) \mathbf{P} \cdot (\hat{\mathbf{k}} \times \hat{\mathbf{E}})$, where $\hat{\mathbf{E}}$ is the electric-field vector, $\mathbf{P}$ is the spin-polarization vector ($|\mathbf{P}| \leq 1$), and $\hat{\mathbf{k}}$ is the observation direction. The resulting asymmetry is approximately proportional to the level-width Γ of the $2p_{1/2}$ state in He$^+$. The improvement is made possible by using a much more reliable photon-detection technique and by a method of data collection and analysis which is self-testing for most systematic errors.

The experiment provides a significant test of radiation theory for hydrogenic ions where lifetimes can be calculated from first principles, but where there have been no previous experimental checks significantly better than $\pm 1\%$ [6], with the exception of an indirect measurement by Sokolov and co-workers [7]. Such tests are of current interest because high-precision ($\pm 0.15\%$) measurements of the lifetime in neutral Li and Na exist which differ from theory by more than five standard deviations [8].

In Sec. II we review the angular distribution of the quench radiation, and in Sec. III we discuss in detail the asymmetry resulting from the finite level width. Sections IV and V describe the experimental method, followed by the results in Sec. VI, and discussion and conclusions in Sec. VII.

II. QUENCHING RADIATION THEORY

A. Ly-α intensity

The theory of electric-field quenching has been described in detail in Refs. [1] and [2]. Here we summarize only the results required for the interpretation of the present experiment. When the quench radiation is observed with photon-polarization-insensitive detectors, the emitted intensity depends on the relative orientation of the three vectors $\mathbf{k}$, $\mathbf{P}$, and $\mathbf{E}$, where $\mathbf{k}$ is the photon wave vector ($|\mathbf{k}| = \omega/c$). The emitted intensity per unit solid angle in an arbitrary observation direction is then of the form

$$I(\hat{\mathbf{k}}) = \frac{\alpha k}{4\pi} [I_0(\hat{\mathbf{k}}) + \mathbf{P} \cdot \mathbf{J}_0] , \tag{1}$$

where

$$I_0(\hat{\mathbf{k}}) = \tfrac{1}{2} |V_{1/2} + 2V_{3/2}|^2 [1 - (\hat{\mathbf{k}} \cdot \hat{\mathbf{E}})^2]$$
$$+ \tfrac{1}{2} |V_{1/2} - V_{3/2} + M_{3/2}|^2 [1 + (\hat{\mathbf{k}} \cdot \hat{\mathbf{E}})^2]$$
$$+ |M_{1/2}|^2 - 4|M_{3/2}|^2 (\hat{\mathbf{k}} \cdot \hat{\mathbf{E}})^2 , \tag{2}$$

$$\mathbf{J}_0 = (\hat{\mathbf{k}} \times \hat{\mathbf{E}}) \{ \text{Re}[M_{1/2}^*(2V_{1/2} + V_{3/2} + M_{3/2})]$$
$$- 3(\hat{\mathbf{k}} \cdot \hat{\mathbf{E}}) \text{Im}[V_{1/2}^*(V_{3/2} + M_{3/2})] \} . \tag{3}$$

The $V_{1/2}$ and $V_{3/2}$ coupling coefficients represent the amplitudes for the electric-field quenching of the $2s_{1/2}$ state via the admixture of the $2p_{1/2}$ and $2p_{3/2}$ intermediate states, respectively, with the emission of an electric dipole ($E1$) photon. $M_{1/2}$ and $M_{3/2}$ are the amplitudes for spontaneous magnetic dipole ($M1$) transitions from the $2s_{1/2}$ to the $1s_{1/2}$ ground state and for magnetic quadrupole ($M2$) transitions via the $2p_{3/2}$ state. To lowest order in the field strength $F = |\mathbf{E}|$, the various amplitudes are given in terms of reduced matrix elements by

$$V_{1/2} = -\frac{b_{1/2}(F)}{4\pi^{1/2}} \langle 1s_{1/2} \| \boldsymbol{\alpha} \cdot (\mathbf{a}_1^{(1)})^* \| 2p_{1/2} \rangle , \qquad (4a)$$

$$V_{3/2} = -\frac{b_{3/2}(F)}{4(2\pi)^{1/2}} \langle 1s_{1/2} \| \boldsymbol{\alpha} \cdot (\mathbf{a}_1^{(1)})^* \| 2p_{3/2} \rangle , \qquad (4b)$$

$$M_{1/2} = \frac{ia(F)}{4\pi^{1/2}} \langle 1s_{1/2} \| \boldsymbol{\alpha} \cdot (\mathbf{a}_1^{(0)})^* \| 2s_{1/2} \rangle , \qquad (4c)$$

$$M_{3/2} = -\frac{b_{3/2}(F)}{4(2\pi/3)^{1/2}} \langle 1s_{1/2} \| \boldsymbol{\alpha} \cdot (\mathbf{a}_2^{(0)})^* \| 2p_{3/2} \rangle , \qquad (4d)$$

where

$$a(F) = 1 + O(F^2) , \qquad (5a)$$

$$b_{1/2}(F) = \frac{eF \langle 2p_{1/2} \| \mathbf{r} \| 2s_{1/2} \rangle}{\sqrt{6}(\mathcal{L} + i\Gamma/2)} + O(F^3) , \qquad (5b)$$

$$b_{3/2}(F) = \frac{eF \langle 2p_{3/2} \| \mathbf{r} \| 2s_{1/2} \rangle}{\sqrt{6}(\mathcal{F} + i\Gamma/2)} + O(F^3) . \qquad (5c)$$

Values for the reduced matrix elements are given in Table I. Here α is the 4×4 Dirac matrix and the $\mathbf{a}_{L,M}^{(\lambda)}$ are the standard operators for electric and magnetic multipole transitions in the Coulomb gauge. The energies in the denominators of the b coefficients are related to the Lamb shift and fine-structure splitting by

$$\mathcal{L} = E(2s_{1/2}) - E(2p_{1/2}) \qquad (6a)$$

and

$$\mathcal{F} = \mathcal{L} - E(2p_{3/2}) + E(2p_{1/2}) . \qquad (6b)$$

The first two terms in $I_0(\hat{\mathbf{k}})$ represent the dominant electric-field quenching process. In the limit of weak electric fields, these are both proportional to the square of the applied field through the b coefficients in Eq. (4). The last two terms are small enough that they may be ignored altogether.

The first term in $\mathbf{J}_0$ represents an interference between the spontaneous $M1$ amplitude and the field-induced quench radiation described by the V coefficients. This term, which is linear in $\hat{\mathbf{k}} \times \hat{\mathbf{E}}$, does not contribute because each signal measurement is averaged over the directions $\hat{\mathbf{E}}$ and $-\hat{\mathbf{E}}$. The intensity that remains after

field averaging is

$$I(\hat{\mathbf{k}}) = \frac{\alpha k}{4\pi} \{ I_0(\hat{\mathbf{k}}) - 3(\mathbf{P} \cdot \hat{\mathbf{k}} \times \hat{\mathbf{E}})(\hat{\mathbf{k}} \cdot \hat{\mathbf{E}})$$
$$\times \mathrm{Im}[V_{1/2}^*(V_{3/2} + M_{3/2})] \} . \qquad (7)$$

The last term in Eq. (7) is called the $E1$-$E1$ damping interference term because it comes primarily from the imaginary part of the cross product $V_{1/2}^* V_{3/2}$. It therefore depends on the imaginary level width contained in the denominators of the V coefficients in Eq. (4).

B. Angular distributions

The geometry of the experiment is such that $\mathbf{P}$ and $\hat{\mathbf{E}}$ are orthogonal and $\hat{\mathbf{k}}$ lies in the plane through $\hat{\mathbf{E}}$ as shown in Fig. 1, where the beam of $\mathrm{He}^+(2s)$ ions travels in the $+\hat{\mathbf{y}}$ direction and θ is the angle between $\hat{\mathbf{E}}$ and $\mathbf{k}$. If the intensity in the direction $\theta = \pi/2$ is renormalized to unity, then the I_0 term in Eq. (7), denoted as the Lamb-shift term, has the angular distribution

$$\mathcal{L}(\theta) = 1 + \frac{2R}{1-R} \cos^2\theta , \qquad (8)$$

where

$$R = \frac{I(0) - I(\pi/2)}{I(0) + I(\pi/2)} \qquad (9)$$

is the Lamb-shift anisotropy used previously [3] to measure the Lamb shift. The second term in Eq. (7) has the angular distribution $(\mathbf{P} \cdot \hat{\mathbf{k}} \times \hat{\mathbf{E}})(\hat{\mathbf{k}} \cdot \hat{\mathbf{E}}) = \frac{1}{2}|\mathbf{P}|\cos\theta\sin\theta$ and with the same normalization, this damping term can be written as

$$\gamma(\theta) = \frac{\pm 2A |\mathbf{P}| \cos\theta \sin\theta}{(1-R)} , \qquad (10)$$

where

$$A = \frac{I(\pi/4) - I(3\pi/4)}{I(\pi/4) + I(3\pi/4)} \qquad (11)$$

is the damping asymmetry. The $(+)$ sign in (10) applies if $\mathbf{P}$ is oriented as shown in Fig. 1 and the $(-)$ sign applies

TABLE I. Summary of transition matrix elements.

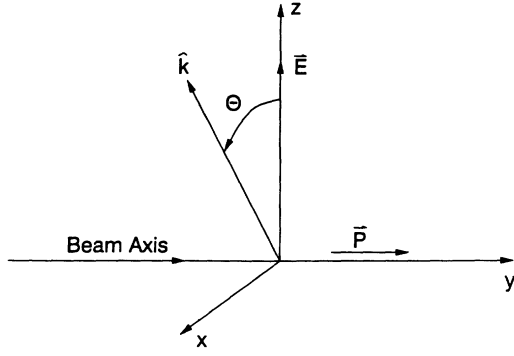| Matrix element	Value
$\langle 2p_{1/2} \| \mathbf{r} \| 2s_{1/2} \rangle$	$3\sqrt{2}a_0 Z^{-1}(1 - \frac{5}{12}\alpha^2 Z^2)$
$\langle 2p_{3/2} \| \mathbf{r} \| 2s_{1/2} \rangle$	$-6a_0 Z^{-1}(1 - \frac{1}{6}\alpha^2 Z^2)$
$\langle 1s_{1/2} \| \boldsymbol{\alpha} \cdot (\mathbf{a}_1^{(1)})^* \| 2p_{1/2} \rangle$	$(ika_0/Z)(2\pi/3)^{1/2}(2^9/3^5)[1 - (\frac{11}{96} + \frac{3}{2}\ln2 - \ln3)\alpha^2 Z^2]$
$\langle 1s_{1/2} \| \boldsymbol{\alpha} \cdot (\mathbf{a}_1^{(1)})^* \| 2p_{3/2} \rangle$	$-(ika_0/Z)(4\pi/3)^{1/2}(2^9/3^5)[1 - (\frac{11}{48} + \frac{5}{4}\ln2 - \frac{3}{4}\ln3)\alpha^2 Z^2]$
$\langle 1s_{1/2} \| \boldsymbol{\alpha} \cdot (\mathbf{a}_1^{(0)})^* \| 2s_{1/2} \rangle$	$ka_0 Z^2 \alpha^3 (4\pi)^{1/2}(2/3)^4(1 + 0.4193\alpha^2 Z^2)$
$\langle 1s_{1/2} \| \boldsymbol{\alpha} \cdot (\mathbf{a}_2^{(2)})^* \| 2p_{3/2} \rangle$	$i(ka_0)^2 Z^{-1} \alpha \pi^{1/2}(2^8/3^5)(1 - 0.1821\alpha^2 Z^2)$
$\langle 2p_{1/2} \| z \| 2s_{1/2} \rangle$	$\sqrt{3}a_0 Z^{-1}(1 - \frac{5}{12}\alpha^2 Z^2)$
$\langle 2p_{3/2} \| z \| 2s_{1/2} \rangle$	$-\sqrt{6}a_0 Z^{-1}(1 - \frac{1}{6}\alpha^2 Z^2)$
$\langle 1s \| z \| 2p \rangle$	$2^7\sqrt{2}a_0 Z^{-1}/3^5$
$\langle 2p \| z \| 2s \rangle$	$-3a_0 Z^{-1}$

FIG. 1. Geometry of the experiment, showing the electric-field vector **E** in the $\hat{z}$ direction, the spin-polarization vector **P** in the $\hat{y}$ direction, and the direction of observation $\hat{k}$ in the xz plane.
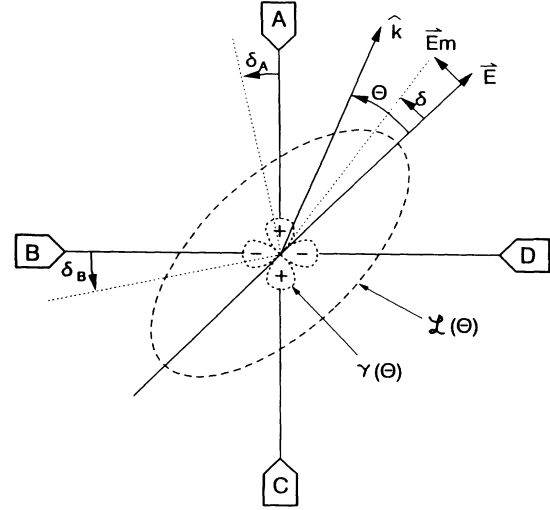

FIG. 2. Polar diagram of the two main contributions to the quench radiation for a spin-polarized He$^+$(2s) beam traveling through the origin into the page for a spin-polarization vector $\hat{P}$ parallel to the beam velocity. $\mathcal{L}(\theta)$ and $\gamma(\theta)$ represent the main quench radiation and the $E1$-$E1$ damping radiation. Photon detectors A, B, C, and D have viewing axes at $\theta = \pi/4$, $3\pi/4$, $5\pi/4$, and $7\pi/4$ from the **E** direction, respectively. Angles δ_A and δ_B are misalignment errors for the viewing axes and δ is the rotation angle of **E** by a small motional field $\mathbf{E}_m = \mathbf{v} \times \mathbf{B}/c$ for a magnetic field **B** along the beam axis.

if **P** is reversed. The total field-reversed average intensity can now be expressed as

$$I(\theta) = \mathcal{L}(\theta) + \gamma(\theta) . \tag{12}$$

A polar diagram of $\mathcal{L}(\theta)$ and $\gamma(\theta)$ is shown in Fig. 2 where the anisotropy in $\mathcal{L}(\theta)$ and the relative magnitude of $\gamma(\theta)$ have been exaggerated. The He$^+$ ion beam passes through the origin into the page with $\hat{P} = +\hat{v}$. The four photon detectors A, B, C, and D view the radiation simultaneously. The radiation patterns are invariant under reversal of $\hat{E}$, but $\gamma(\theta)$ reverses sign if $\hat{E}$ is rotated by $\pi/2$ or **P** is reversed. $\mathcal{L}(\theta)$ is invariant under both of these operations along the detector viewing axis at $\theta = \pi/4$, $3\pi/4$, $5\pi/4$, and $7\pi/4$.

III. THE DAMPING ASYMMETRY

A. The weak-field limit

Substituting $I(\hat{k})$ from Eq. (7) into the definition of A yields

$$A = \frac{-3 \, \mathrm{Im}[V_{1/2}^*(V_{3/2} + M_{3/2})]}{\frac{1}{2}|V_{1/2} + 2V_{3/2}|^2 + \frac{3}{2}|V_{1/2} - V_{3/2}|^2 - \mathrm{Re}[M_{3/2}^*(V_{1/2} - V_{3/2})]} . \tag{13}$$

For purposes of presenting the results, the small $M_{3/2}$ corrections will be temporarily dropped, and then included later as a perturbation. With $M_{3/2}$ omitted, A can be written in the form

$$A = \frac{-3 \, \mathrm{Im}(\rho)}{2 - \mathrm{Re}(\rho) + 7|\rho|^2} , \tag{14}$$

where ρ is the fundamental ratio

$$\rho = V_{3/2}/V_{1/2} . \tag{15}$$

Similarly, in the limit of weak fields and nonrelativistic matrix elements, ρ reduces to the zero-order quantity

$$\rho_0 = \frac{\mathcal{L} + i\Gamma/2}{\mathcal{J} + i\Gamma/2} , \tag{16}$$

and the corresponding zero-order asymmetry becomes [4]

$$A_0 = \frac{3\Gamma|\mathbf{P}|(\mathcal{L} - \mathcal{J})}{4\mathcal{J}^2 - 2\mathcal{L}\mathcal{J} + 7\mathcal{L}^2 + 9\Gamma^2/4} , \tag{17}$$

independent of field strength F. It is evident that a measurement of A_0 is equivalent to a measurement of Γ since the energy differences, defined by Eq. (6), are known to high precision. Using the data in Table II,

TABLE II. Data for calculating the asymmetry A_0 in the limit of weak fields.

Quantity	Value
$E(2s_{1/2}) - E(2p_{1/2})$	14 042.51 MHz
$E(2p_{3/2}) - E(2p_{1/2})$	175 593.54 MHz
$\gamma(2p)$	1.003 118 $\times 10^{10}$ rad/sec

$A_0 = 0.007\,623\,135$. The corrections due to finite electric-field strengths, relativistic effects, and the $M_{3/2}$ term are discussed in the following sections.

B. Small corrections

1. Finite-field correction

Finite electric fields introduce higher-order perturbation corrections to the mixing coefficients $a(F)$, $b_{1/2}(F)$, and $b_{3/2}(F)$ in Eq. (4), which carry over into the V_j coefficients and to ρ. The coefficients in the expansion

$$\rho = \rho_0 + F^2 \rho_2 + F^4 \rho_4 + \cdots \tag{18}$$

are given by [1]

$$\rho_2 = 3 \left[\frac{ea_0}{Z(\mathcal{L} + i\Gamma/2)} \right]^2 \rho_0 (1 + 2\rho_0)(1 - \rho_0) , \tag{19}$$

$$\rho_4 = -3 \left[\frac{ea_0}{Z(\mathcal{L} + i\Gamma/2)} \right]^2 \rho_2 (1 + \rho_0 + 4\rho_0^2) , \tag{20}$$

where a_0 is the Bohr radius. Using these, the A expansion is

$$A = A_0 + A_2 F^2 + A_4 F^4 + \cdots , \tag{21}$$

where

$$A_2 = A_0 \{ 3\,\mathrm{Im}(\rho_2) + A_0 [7\,\mathrm{Re}(\rho_0^* \rho_2) - \mathrm{Re}(\rho_2)] \} / 3\,\mathrm{Im}(\rho_0) , \tag{22}$$

$$A_4 = A_0 \{ 3\,\mathrm{Im}(\rho_4) + A_0 [7\,\mathrm{Re}(\rho_0^* \rho_4) - \mathrm{Re}(\rho_4) + \tfrac{7}{2} |\rho_2|^2] \} / 3\,\mathrm{Im}(\rho_0) . \tag{23}$$

To separate the real and imaginary parts in the ρ expansion, define

$$\epsilon = -\mathcal{L}/\mathcal{F} . \tag{24}$$

Then, to second order in $\Gamma/\mathcal{L}$, the A coefficients are

$$A_2 = -\frac{3A_0 F_0^2}{1+\epsilon} \left\{ 1 - \epsilon + 4\epsilon^2 + 6\epsilon^3 + \tfrac{2}{3} A_0 \frac{\mathcal{L}}{\Gamma} \left[1 + 6\epsilon - 7\epsilon^2 - 14\epsilon^3 - \frac{1}{4} \left[\frac{\Gamma}{\mathcal{L}} \right]^2 (1 + 13\epsilon + 15\epsilon^2) \right] \right\} , \tag{25}$$

$$A_4 = \frac{9A_0 F_0^4}{1+\epsilon} \left\{ 3 - 5\epsilon + 7\epsilon^2 - 9\epsilon^3 + 16\epsilon^4 + 40\epsilon^5 + \tfrac{2}{3} A_0 \frac{\mathcal{L}}{\Gamma} \left[1 + \tfrac{3}{2}\epsilon - 4\epsilon^2 + 26\epsilon^3 - 26\epsilon^4 - 70\epsilon^5 \right. \right.$$
$$\left. \left. - \frac{1}{4} \left[\frac{\Gamma}{\mathcal{L}} \right]^2 (6 + \tfrac{99}{2}\epsilon - 54\epsilon^2 + 2\epsilon^3 + 152\epsilon^4 - 14\epsilon^5) \right] \right\} , \tag{26}$$

where

$$F_0^2 = \left[\frac{ea_0}{Z\mathcal{L}} \right]^2 .$$

Using the data in Table II, the numerical values are

$$A_2 = -4.4025 \times 10^{-11} \ (\mathrm{V/cm})^{-2} ,$$

$$A_4 = 7.2427 \times 10^{-19} \ (\mathrm{V/cm})^{-4} .$$

Since $|A_2| \gg |A_4|$, A decreases as F increases in the limit of weak fields. The physical reason is that the electric-field-perturbed $2p$ state is mixed with the longer-lived $2s$ state.

2. Magnetic quadrupole correction

The fractional correction $(\delta A / A_0)_{M2}$ due to the $M_{3/2}$ magnetic quadrupole terms in Eq. (13) can be simply expressed in terms of ratios of matrix elements. Defining $\sigma = M_{3/2}/V_{1/2}$, then

$$(\delta A / A_0)_{M2} = [\mathrm{Im}(\sigma) - \tfrac{1}{3} A_0 \mathrm{Re}(\sigma)$$
$$+ \tfrac{1}{3} A_0 |\rho|^2 \mathrm{Re}(\sigma/\rho)] / \mathrm{Im}(\rho) . \tag{27}$$

Using Eq. (4) and the matrix elements in Table I,

$$(\delta A / A_0)_{M2} = -\tfrac{9}{32}(\alpha Z)^2 \left[1 - \tfrac{1}{3} A_0 \frac{\mathrm{Re}(\rho) - |\rho|^2}{\mathrm{Im}(\rho)} \right] , \tag{28}$$

which to second order in $\Gamma/\mathcal{L}$ becomes

$$(\delta A / A_0)_{M2} = -\tfrac{9}{32}(\alpha Z)^2 (1 - \tfrac{2}{3} A_0 \mathcal{L}/\Gamma) . \tag{29}$$

For He^+, the numerical value is

$$(\delta A / A_0)_{M2} = -5.7230 \times 10^{-5} . \tag{30}$$

3. Relativistic corrections to matrix elements

The relativistic corrections to the matrix elements of order $0(\alpha^2 Z^2)$ in Table I carry over into the V coefficients of Eq. (4). Denoting the fractional corrections to the matrix elements $\langle 2p_j \| \mathbf{r} \| 2s_{1/2} \rangle$ and $\langle 1s_{1/2} \| \boldsymbol{\alpha} \cdot (\mathbf{a}_1^{(1)})^* \| 2p_j \rangle$ by μ_j and μ_j', respectively, for $j = \tfrac{1}{2}$ and $\tfrac{3}{2}$, the values from Table I are

$$\mu_{1/2} = -5(\alpha Z)^2/12, \quad \mu_{3/2} = -5(\alpha Z)^2/12 ,$$

$$\mu_{1/2}' = (-\tfrac{11}{96} - \tfrac{1}{2}\ln 2 + \ln 3)(\alpha Z)^2 , \tag{31}$$

$$\mu_{3/2}' = (-\tfrac{11}{48} - \tfrac{5}{4}\ln 2 + \tfrac{3}{4}\ln 3)(\alpha Z)^2 .$$

A further complication is that the $i\Gamma$ terms in the denominators of $b_{1/2}(F)$ and $b_{3/2}(F)$ defined in Eqs. (5b) and (5c) are actually $i\Gamma_{1/2}$ and $i\Gamma_{3/2}$, with $\Gamma_{1/2} = \Gamma_{3/2}$ in the nonrelativistic limit. Since $\Gamma_j \sim \Delta E_j |\langle 1s_{1/2}||\alpha \cdot (\mathbf{a}_1^{(1)})^*||2p_j\rangle|^2$, the relativistic correction factors are of the form $(1+\mu_j'')$ with $\mu_{1/2}'' = 11(\alpha Z)^2/48 + 2\mu_{1/2}'$ and $\mu_{3/2}'' = 15(\alpha Z)^2/48 + 2\mu_{3/2}'$. The experiment is predominantly sensitive to $\Gamma_{1/2}$, and so we will write $\Gamma_{1/2} = \Gamma$, with $\Gamma_{3/2}$ related to Γ by

$$\Gamma_{3/2} = \Gamma(1 + \mu_{3/2}'' - \mu_{1/2}'') . \tag{32}$$

Defining $\mu = \mu_{3/2} - \mu_{1/2}$, and similarly for μ' and μ'', the correction factor is

$$(\delta A / A_0)_{\mathrm{rel}} = \mu + \mu' + \mu'' \frac{\Gamma \,\mathrm{Re}(\rho_0)}{4\mathscr{F}\,\mathrm{Im}(\rho_0)}$$

$$+ (\mu + \mu')[7|\rho_0|^2 - \mathrm{Re}(\rho_0)]\frac{A_0}{\mathrm{Im}(\rho_0)} \tag{33}$$

or, to first order in $\Gamma/\mathcal{L}$,

$$(\delta A / A_0)_{\mathrm{rel}} = \mu + \mu' + \mu'' \left[\frac{\epsilon}{1+\epsilon} \right]$$

$$+ (\mu + \mu')A_0 \left[\frac{2\mathcal{L}}{3\Gamma} \right]\left[\frac{1+7\epsilon}{1+\epsilon} \right] . \tag{34}$$

For He$^+$, the correction is

$$(\delta A / A_0)_{\mathrm{rel}} = -8.36 \times 10^{-7} . \tag{35}$$

4. Mixing with higher np states and final-state perturbations

The mixing of the $2s_{1/2}$ state with higher np states ($n > 2$) and perturbation of the $1s_{1/2}$ final state can be described in terms of the coefficients

$$B = \sum_{n=3}^{\infty} \frac{\langle 1s|z|np\rangle\langle np|z|2s\rangle}{E(2s) - E(np)} , \tag{36}$$

$$C = \sum_{n=2}^{\infty} \frac{\langle 1s|z|np\rangle\langle np|z|2s\rangle}{E(1s) - E(np)} , \tag{37}$$

which have an obvious meaning analagous to the V coefficients of Eq. (4). Using the method of Dalgarno and Lewis [9], they can be calculated analytically with the result [1,10]

$$B = -25[2^9/(3^6\sqrt{2})]a_0^3/e^2, \quad C = 7[2^9/(3^6\sqrt{2})]a_0^3/e^2 .$$

The effects of these terms is to add a small additional $E1$ quenching background which can be taken into account by replacing the $V_{1/2} + 2V_{3/2}$ term in Eq. (2) by $V_{1/2} + 2V_{3/2} - ikeF(B+C)$. Recall that the V_j coefficients themselves are proportional to F so that, in lowest order, the overall field dependence is unchanged. From Eq. (13) the fractional correction to the asymmetry is

$$(\delta A / A_0)_{np} = -\tfrac{1}{3}A_0 ke(B + C)$$

$$\times \mathrm{Im}(V_{1/2} + 2V_{3/2})/\mathrm{Im}(V_{1/2}^* V_{3/2}) . \tag{38}$$

To second order in $\Gamma/\mathcal{L}$, this becomes

$$(\delta A / A_0)_{np} = 3A_0 Z^4 \left[\frac{\mathcal{L}}{\hbar\omega} \right]\left[\frac{\mathcal{L}}{\Gamma} \right]$$

$$\times \left[\frac{1 - 2\epsilon - \Gamma^2/(4\mathcal{L}^2)}{\epsilon(1+\epsilon)} \right] , \tag{39}$$

where $\hbar\omega = 3Z^2/4$ Ry is the $2s$-$1s$ transition frequency. For He$^+$, the numerical value is

$$(\delta A / A_0)_{np} = -39.99 \times 10^{-6} . \tag{40}$$

C. Overall correction

The sum of the corrections in Secs. III B 1–III B 4 to the uncorrected $A_0 = 7.623\,1349 \times 10^{-3}$ is shown in Table III for our operating fields of 492.2 and 532.2 V/cm. Most of our data were obtained at 492.2 V/cm, where Eqs. (8) and (10) reduce to

$$\mathcal{L}(\theta) = 1.267\,88\cos^2\theta ,$$

$$\gamma(\theta) = \pm 0.017\,263\,9|\mathbf{P}|\cos\theta\sin\theta .$$

The relatively strong field dependence for $\gamma(\theta)$ requires that the field be well known in a precision experiment. The last column in Table III will be discussed in Sec. III D 2.

D. Motional electric-field effects

During the experiment the spin-polarization vector for the He$^+$(2s) ions in the beam is set either parallel ($\hat{\mathbf{P}} = +\hat{\mathbf{v}}$) or antiparallel ($\hat{\mathbf{P}} = -\hat{\mathbf{v}}$) to the beam velocity by a spin polarizer [4] before the ions enter the observation cell, as described in Sec. IV. An applied axial magnetic field in the direction of $\mathbf{P}$ then ensures that the alignment of the spin vector with the beam axis is maintained. For magnetic fields $B > 10$ G, depolarization by Larmor precession about remaining stray fields (~ 1 mG) is negligible.

As the ions transverse the electric quenching field (see Fig. 1) they gradually acquire a small transverse velocity $v_\perp$ in the direction of $\mathbf{E}$ before they reach the observation region along the beam axis. The transverse velocity results in a small motional electric field $\mathbf{E}_m = \mathbf{v}_\perp \times \mathbf{B}/c$, where $\mathbf{B}$ is the axial magnetic field. When $\mathbf{E}_m$ is added to the applied field $\mathbf{E}$ the direction of the resultant field is rotated through a small angle

$$\delta = v_\perp B /(cF) , \tag{41}$$

where $F = |\mathbf{E}|$. Since in our experiment $v_\perp/v \sim 10^{-4}$, $B \sim 30$ G, and $F \sim 500$ V/cm, one finds $|\delta| \sim 2 \times 10^{-3}$ rad.

Upon rotation of the electric field, the asymmetry for adjacent detectors, say A and B in Fig. 2, becomes

$$A' = \frac{I(\pi/4-\delta)-I(3\pi/4-\delta)}{I(\pi/4-\delta)+I(3\pi/4-\delta)} \, . \tag{42}$$

Using Eqs. (12), (8), and (10) with $|\mathbf{P}|=1$, one finds

$$A' = A(1-2\sin^2\delta)+R\sin2\delta \, , \tag{43}$$

which to sufficient accuracy may be approximated by

$$A' = A + 2R|\delta| \, . \tag{44}$$

The appearance of $|\delta|$ ensures the validity of the equation for both spin-polarization directions $\hat{\mathbf{P}}=\hat{\mathbf{v}}$ and $-\hat{\mathbf{v}}$. The reason is that when the direction of $\hat{\mathbf{P}}$ is reversed, $\gamma(\theta)$ changes sign but also δ changes sign by the required reversal of the magnetic-field direction. Substitution of Eq. (41) gives

$$A' = A + 2R\left|\frac{v_\perp B}{cF}\right| \, , \tag{45}$$

showing that A' increases linearly with B for both $\hat{\mathbf{P}}=\hat{\mathbf{v}}$ and $-\hat{\mathbf{v}}$. A itself depends weakly on B, as shown by Eq. (51) in Sec. III D 2, but this can be ignored.

E. Misalignment effects

1. Effect on the asymmetry

The derivation of Eq. (43) assumes that the central viewing axes of the adjacently mounted detectors, such as A and B in Fig. 2, are precisely located at 45° and 135° from the direction of the applied electric field. However, machining tolerances for the construction of the apparatus allow a latitude of 2×10^{-4} to 3×10^{-4} rad. Denoting these by δ_A and δ_B for detectors A and B, the observed asymmetry for $\hat{\mathbf{P}}=\pm\hat{\mathbf{v}}$ becomes

$$A^\pm = A + R\left[A(\delta_A-\delta_B)\mp(\delta_A+\delta_B)+2\left|\frac{v_\perp B}{cF}\right|\right] \tag{46}$$

to first order in the δ's. With $\hat{\mathbf{P}}=-\hat{\mathbf{v}}$, the uncertainty in A^+, resulting from the misalignment uncertainties, arises mainly from the second term inside the large parentheses. With $R=0.110$, $A=7.6\times10^{-3}$, and $(\delta_A+\delta_B)\lesssim5\times10^{-4}$, the error in A^+ can be as large as 0.8%. However, when $\hat{\mathbf{P}}$ is reversed to $\hat{\mathbf{P}}=-\hat{\mathbf{v}}$, the sign of the $(\delta_A+\delta_B)$ term changes and so it cancels on taking the average. The much smaller $A(\delta_A-\delta_B)$ term in Eq. (45) can be ignored, leaving

$$A_{av} = A + 2R\left|\frac{v_\perp B}{cF}\right| \tag{47}$$

for the average, in agreement with Eq. (45). Ignoring the $A(\delta_A-\delta_B)$ term introduces a relative error $\delta A/A$ of at most 60 parts per million (ppm).

In the experiment, A_{av} is measured as a function of the magnetic-field strength B, and the limit found by extrapolation to $B=0$. The precision in the A value thus found is in principal limited to about 60 ppm for our apparatus.

2. Effect on the damping ratio

As will be discussed in Sec. V, the quantity directly measured in the experiment is the damping intensity ratio defined by $r=I(\pi/4)/I(3\pi/4)$, or equivalently,

$$r=(1+A)/(1-A) \, . \tag{48}$$

The electric-field dependence of r is shown as the last column of Table III. Substituting Eq. (46) into (48), the magnetic-field and misalignment corrections now appear in the form

$$r^\pm(B)=r+2Rr\left[\mp(\delta_A+\delta_B)+2\left|\frac{v_\perp B}{cF}\right|\right] \tag{49}$$

for $\hat{\mathbf{P}}=\pm\hat{\mathbf{v}}$, and the small $A(\delta_A-\delta_B)$ has again been ignored. The slope with respect to B is

$$\frac{dr^\pm}{dB}\simeq4Rr\frac{v_\perp}{cF}+\frac{\partial r}{\partial B} \, , \tag{50}$$

where the last term is the implicit dependence of r on B due to the perturbing effect of the magnetic field on the atomic wave functions. A direct numerical calculation involving an exact diagonalization of the Hamiltonian in the external fields gives

$$\frac{\partial r}{\partial B}=(-0.1755-5.3\times10^{-6}B$$
$$+0.02486F^2)\times10^{-6}\ \mathrm{G}^{-1} \, , \tag{51}$$

with F in kV/cm and B in Gauss.

In the extrapolated limit $B\to0$, the difference $\Delta r=r^+(0)-r^-(0)$ becomes

$$\Delta r=4rR(\delta_A+\delta_B) \, . \tag{52}$$

This is a particularly useful result because Δr provides a direct measure of alignment errors in the observation axes of the adjacently mounted detectors A and B. The experiment is therefore self-checking for this systematic error. With our alignment tolerances of $|\delta_A+\delta_B|<5\times10^{-4}$, the expected difference is $\Delta r<2.5\times10^{-4}$.

IV. EXPERIMENTAL METHOD

A. Observation cell

Figure 3 shows a cross section of the observation cell which has previously been described in detail [3]. A 10-μA He$^+$ ion beam of energy 134 ± 1 keV passes through the center of the cell into the page. The beam consists mainly of ground-state ions with a concentration of about 0.5% He$^+$ ions in the metastable $2s$ state. The $2s$ state is formed by passing a beam of ground state He$^+$ ions through a cell containing N_2 gas. After the cell, the beam enters a spin polarizer [4] where the spin-polarization vector can be set to $\hat{\mathbf{P}}=\pm\hat{\mathbf{v}}$ to a high degree of precision. Next it passes through a prequenching stage. Here the He$^+(2s)$ ions can be destroyed, forming He$^+(1s)$ ions, by cylindrically symmetric electric fields on the beam axis. These prequenching fields are normally set to zero And are only switched on for noise determina-
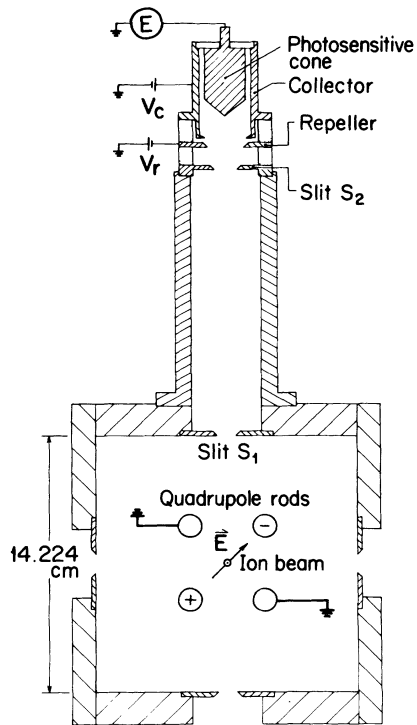
FIG. 3. Cross section of the observation cell showing one of the four identical symmetrically placed photon-detection systems. A dipole field **E** is produced by grounding two of the diagonally located rods and by applying opposite polarities to the other two. The photon-detection system is shown in detail in Fig. 4.

FIG. 4. Details of the photon-detection systems A, B, C, and D shown in Fig. 2. The beam diameter $2p$ is 0.228 cm, the width 2α of the rectangular slit S_1 is 1.245 cm, the diameter 2β of the circular slit S_2 is 1.270 cm. Slits S_2 and S_1 are mounted at distances $s = 21.999$ cm and $c = 7.117$ cm. The beam deflections $(z_0)_1$ and $(z_0)_2$ [see Eq. (53)] due to the transverse-quenching field are exaggerated for clarity.

tions. After the prequencher, the beam is collimated to limit its angular divergence to within 0.1° as it enters the observation region of Fig. 3.

In the observation region, the beam is subjected to a static electric field maintained between four metal rods mounted on insulators in a quadrupole arrangement. Two diagonally located opposite rods are grounded while the other two are given opposite polarities to produce a field that resembles a dipole field. The field direction can readily be rotated through steps of 90° merely by switching polarities. The strength of the dipole field in units of V/cm is $F = 0.3076$ V, where V is the potential in volts on either one of the ungrounded rods.

The electric-field-induced quench radiation of the beam is simultaneously measured by the four detectors A, B, C, and D. Each of these views the emitted radiation at an angle of either $\pi/4$ or $3\pi/4$ from the electric-field direction for any one of its orientations. The solid angle of observation defined by the photon collimator slits S_1 and S_2 is the same for each detector.

B. Photon detection

As previously described [3], each of the four detectors shown in Figs. 2 and 3 is actually a pair of identical detectors placed a distance $l = 3.048$ cm apart along the ion beam, as shown in Fig. 4. After collimation, the Ly-α
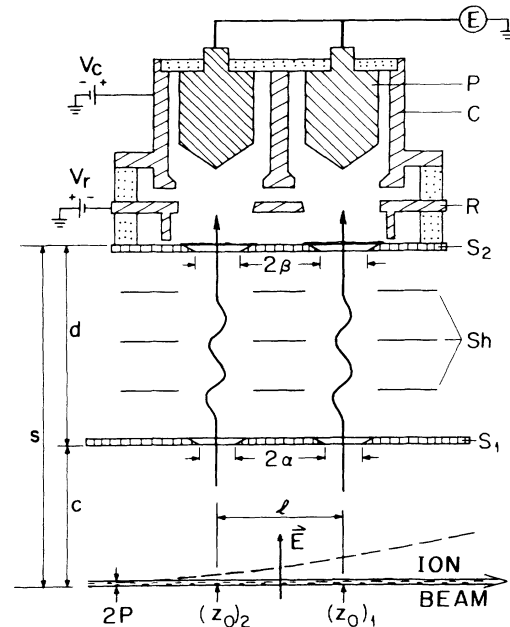
photons from the beam strike a photosensitive cone P that is coated with a layer of MgF_2 to enhance the photoelectric yield. A cylindrical housing is kept at a positive potential (90 V) to collect the photoelectrons. Shields Sh prevent photons from crossing between the collimators.

The combined photoelectric current ($\sim 10^{-13}$ A) of a detector pair is measured with high-precision electrometers (Keithley Model 642 LNFA) without current amplification. The output of the electrometers is proportional to the incident photon current with a high degree of precision of a few parts per million [3]. This should be contrasted to intensity measurements using conventional photon-counting techniques where we have found that current amplification can introduce deviations as large as 1000 ppm for photon fluxes as low as 10^4 per second. The photon flux in the present experiment is about 10^6 photons per second per detector pair.

The analog output of each electrometer is fed to a digital voltmeter (Hewlett Packard Model 3457 A). The voltmeter output, normalized to the beam current, is stored in a computer.

During the measurements of the small photocurrents, one must take care to avoid parasitic currents on the photoconversion cone by stray electrons, low-energy ions, and metastable particles created by collisions of the fast-ion beam with the residual gas (6×10^{-8} Torr). Stray particles are suppressed by the axial magnetic field in the observation region which confines electrons traveling with the beam near its axis and by covering the exit slits S_2 of the photon collimators with thin (~ 500-Å) alumi-

TABLE III. Field dependence of R, A, and $r=(1+A)/(1-A)$.

F (V/cm)	R	A	r
0	0.117 9785	0.007 622 999	1.015 363 11
492.2	0.118 1200	0.007 612 333	1.015 341 44
532.2	0.118 1438	0.007 610 537	1.015 337 80

TABLE V. Predicted slope dr/dB, where $(dr/dB)_0 = 4rRv_\perp/(cF)$ is the first term in Eq. (50).

F (V/cm)	$\left[\dfrac{dr}{dB}\right]_0$ (G^{-1})	$\dfrac{dr}{dB}$ (G^{-1})
492.2	$(28.95\pm0.13)\times10^{-6}$	$(28.75\pm0.13)\times10^{-6}$
532.2	$(28.84\pm0.13)\times10^{-6}$	$(28.68\pm0.13)\times10^{-6}$

num films. The relative efficiencies of the detector pairs differ by about 1% due to small variations in the thickness of the various films. Electrons ejected from the back surface of the films are suppressed by a repeller plate, kept at -300 V.

For axial magnetic fields $B < 13$ G, an electron background can still be detected when the polarities on the quadrupole rods exceed 2000 V, corresponding to an electric field $F > 615$ V/cm. To ensure the absence of possible systematic errors from an electron background current, the electric field is kept below 540 V/cm and the magnetic field is kept above 19 G in all the measurements.

C. The axial magnetic field

The axial magnetic field in the observation region consists of a residual stray magnetic field (~ 5 G) from the spin polarizer and a stronger applied field, in the same direction, from a pair of Helmholtz coils. The stray field is not quite homogeneous but has a small divergence. The divergence in the total magnetic field is reduced to 0.00 G/cm by passing unequal currents through the Helmholtz coils, which are kept constant in time to a precision of 6 parts in 10^4. The maximum total magnetic field obtainable without the risk of damaging the Helmholtz coils by I^2R heating is 40 G. The magnetic field is measured with a Gaussmeter (Bell model 640), whose output is connected to a digital voltmeter. Using electron-spin resonance, we have calibrated the Gauss meter output to an absolute precision of 0.2% and found its linearity to be within 3 parts in 1000. Magnetic-field components perpendicular to the beam axis are canceled over the observation region with auxiliary coils.

D. Transverse-velocity effects

As the beam enters the quenching cell at $y=0$ along the y axis, there is a progressive depletion of the metastable state. The radiation intensity decays along the beam according to $I(y)=I_0e^{-\gamma y}$, where $1/\gamma$ is the decay length due to quenching. The beam also bends due to the transverse electric field, giving it a parabolic trajectory of the form

$$z=z_0+\lambda y+\mu y^2 , \tag{53}$$

where z_0 is the beam deflection and $\lambda=v_\perp/v$, all evaluated at the center of the detector viewing area. Finally $\mu=F/4V_a$, where V_a is the accelerating potential for the ion beam.

The small transverse displacements ($z_0 < 0.065$ cm) introduce negligible corrections and may be ignored. The transverse velocities, however, have significant effects on the data analysis. The average transverse velocity $v_\perp$ for a detector pair whose upstream and downstream viewing axes are located at $y_1=6.096$ cm and $y_2=9.144$ cm from the entrance slip must take into account the relative Ly-α intensities w_1 and w_2 at y_1 and y_2, respectively. It is given by

$$v_\perp=\frac{w_1\lambda_1v+w_2\lambda_2v}{w_1+w_2} ,$$

where λ_1 and λ_2 are the relative transverse velocities at y_1 and y_2, respectively.

The computation of $v_\perp$ for the two electric-field values used in the experiment is indicated in Table IV. The error in $v_\perp$ arises from the uncertainty in the absolute beam velocity $v=(2.543\pm0.010)\times10^8$ cm/sec and a 0.2% uncertainty in λ. The details for calculating the latter are described in Ref. [3].

The whole point of calculating $v_\perp$ is to find the slope dr/dB from Eq. (50). Since $r\simeq1.015$ is close to unity, the slope is nearly independent of the A asymmetry, but a measurement of the slope provides a stringent test of the apparatus. A comparison between the predicted and measured slopes provides a test for systematic errors, not only for the damping asymmetry, but also for our previous experiments on the Lamb shift in hydrogenic ions [3].

The slopes dr/dB listed in the second column of Table V were calculated with the input data of Tables III and IV. The last column takes into account the finite solid angle of observation and the higher-order field corrections of Eq. (51). The former has the effect of reducing the Lamb-shift anisotropy R [3], and hence the slope by a factor of 1.0013. Although the field correction itself depends on the magnetic field, the change is only 6 parts in 10^4 in the field range 20–40 G used in the experiment.

TABLE IV. Data for calculating the average transverse velocity $v_\perp$ for the two field values used.

F (V/cm)	γ (cm^{-1})	w_1	w_2	λ_1	λ_2	$v_\perp$ (10^6 cm/sec)
492.2	0.059 67	0.5443	0.4547	0.009 14	0.014 72	2.969$\pm$0.013
532.2	0.067 6	0.5530	0.4470	0.009 88	0.015 92	3.199$\pm$0.014

V. MEASUREMENT TECHNIQUE

The direct measurement of intensity ratios r, instead of asymmetries, avoids the need to determine the relative sensitivities of the detectors. For each measurement, the photocurrents from the detector pairs, normalized to the beam current, are time averaged for 30 sec. The data are then combined in such a way that all significant systematic errors except for magnetic-field effects cancel to first order. The scheme is as follows. Let the angle θ in Fig. 2 specify the direction of observation for any one of the detectors A,B,C,D relative to E, with a consistent sign convention for positive rotation. The field-reversed average current ratio between an adjacent pair of detectors is defined to be

$$r_{AB}^2 = \left| \frac{A(-\pi/4) + A(3\pi/4)}{B(-3\pi/4) + B(\pi/4)} \right|$$
$$\times \left| \frac{B(-\pi/4) + B(3\pi/4)}{A(-3\pi/4) + A(\pi/4)} \right| , \qquad (54)$$

with analogous cyclic permutations for r_{BC}^2, r_{CD}^2, and r_{DA}^2. The summing of currents inside the parentheses guarantees the required field averaging for opposite field directions, discussed in Sec. II.

Next we construct the average

$$r = (r_{AB} + r_{BC} + r_{CD} + r_{DA})/4 \qquad (55)$$

of the four current ratios measured for a given orientation of P and a given magnetic-field strength. Equation (54) must still be corrected for noise defined as the signal still observed after the beam of metastable ions is destroyed with the prequencher. The dc level of the noise current is proportional to the residual pressure in the observation cell. At the operating pressure of 6×10^{-8} Torr, the background noise is 1%.

It is clearly desirable to carry out measurements at more than one electric-field strength, but in fact the range of practical fields is rather limited. An upper limit of $F\sim615$ V/cm arises from the requirement of keeping the background noise from stray electrons under control (see Sec. IV B), and at much lower fields the Ly-α intensity becomes inconveniently small. The two field strengths used of 492.2 and 532.2 V/cm provide at least a limited check for field-dependent systematic effects.

VI. RESULTS

A. Uncorrected data

It was necessary to take data for at least two values of B in order to extrapolate to $B=0$. Histograms for measurements with $F=492.2$ V/cm and $\hat{P}=+\hat{v}$ are shown in Fig. 5. Figures 5(a) shows 1155 measurements at $B=19.19$ G and Fig. 5(b) shows 1011 measurements at $B=38.41$ G. The histograms are well fitted by Gaussian curves. A χ^2 test for Fig. 5(a) yields $\chi^2=19.5$ for 30 degrees of freedom corresponding to a 93% confidence level, while for Fig. 5(b), $\chi^2=31.2$ for 26 degrees of freedom corresponding to a 23% confidence level.

The average values of r are listed in the last column of

TABLE VI. Observed damping ratio at $F=492.2$ V/cm. Numbers in parentheses denote the uncertainties in the final figures quoted.

$\hat{P}$	B (G)	$r(B)$
$+\hat{v}$	19.19	1.015 9103(120)
	38.41	1.016 4636(127)
$-\hat{v}$	19.28	1.015 8153(118)
	38.49	1.016 3565(124)

Table VI, which also presents similar results for $\hat{P}=-\hat{v}$. The slight difference in magnetic-field strengths along the beam axis when $\hat{P}$ is reversed results from stray fields. Only stray fields perpendicular to the beam axis are canceled.

The magnetic-field dependence of r is shown in Fig. 6, where the extrapolated values to zero magnetic field are

$$r^+(0) = 1.015\,357\,84 \pm 0.000\,027\,2 ,$$

$$r^-(0) = 1.015\,272\,21 \pm 0.000\,026\,7 .$$

The difference $\Delta r = (0.86\pm0.38)\times10^{-4}$ is due to alignment errors, as further discussed at the end of this section. The final average over spin-polarization vectors yields

$$r(0) = 1.015\,315\,0 \pm 0.000\,019\,0 .$$
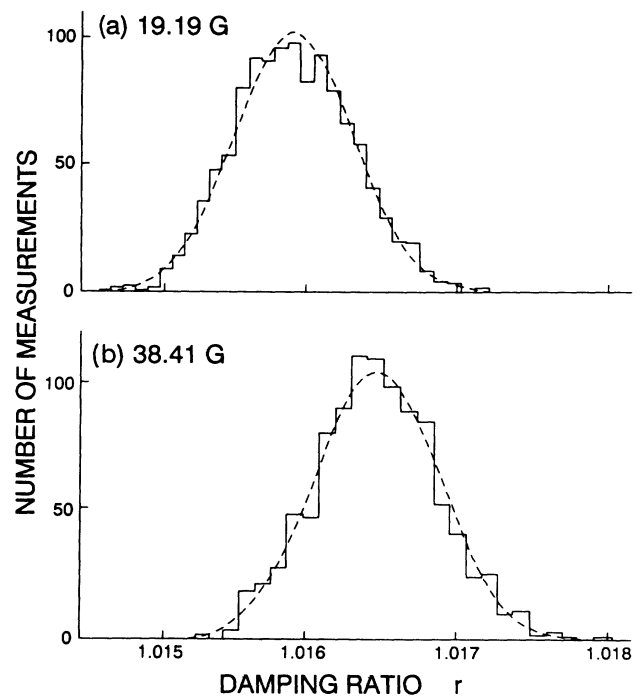
The slopes of the straight lines in Fig. 6 are

FIG. 5. Histograms for the distribution of the experimental data with $\hat{P}=+\hat{v}$ and a quenching field $F=492.2$ V/cm for (a) an axial-magnetic field of 19.19 G for a total of 1155 individual measurements and (b) an axial-magnetic field of 38.41 G for a total of 1011 individual measurements. The dotted lines are Gaussian distributions with the same mean and half-widths.
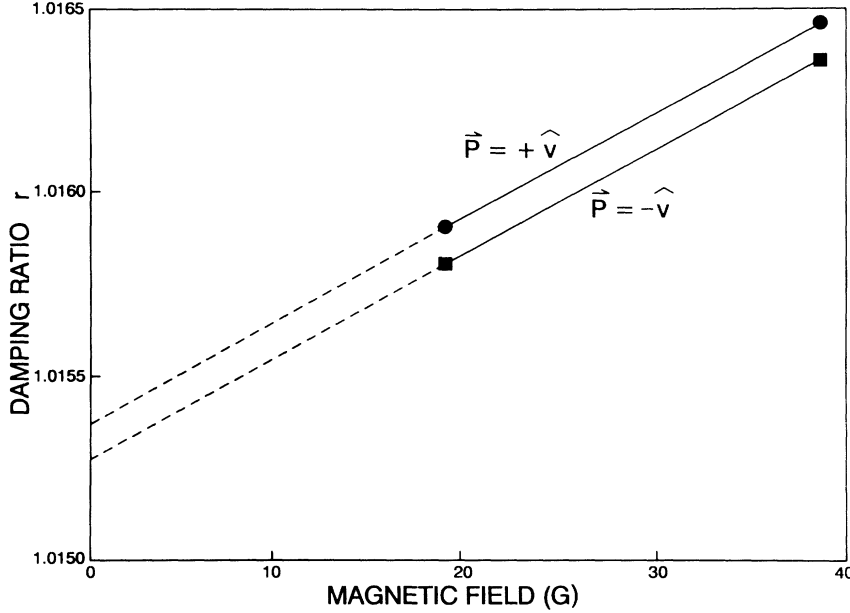
FIG. 6. The magnetic-field dependence of the damping ratio for $\hat{\mathbf{P}} = \pm\hat{\mathbf{v}}$ at a quenching field $F = 492.2$ V/cm.

$$\left[\frac{dr}{dB}\right]^+ = (28.79 \pm 0.91) \times 10^{-6} \text{ G}^{-1} ,$$

$$\left[\frac{dr}{dB}\right]^- = (28.17 \pm 0.89) \times 10^{-6} \text{ G}^{-1} ,$$

with an average of

$$\frac{dr}{dB} = (28.48 \pm 0.64) \times 10^{-6} \text{ G}^{-1} ,$$

in good agreement with the average predicted value

$$\frac{dr}{dB} = (28.75 \pm 0.13) \times 10^{-6} \text{ G}^{-1}$$

from Table V.

The uncertainty in dB/dr takes into account the error bars in Fig. 6 (which are too small to show) and a 0.2% uncertainty in the absolute magnetic field. The extrapolated $r(0)$ values do not depend on uncertainties in the absolute value of B, but only on the linearity of the Gauss meter. Since linearity lies within 3 parts in 10^3, extrapolation errors are negligible.

The optimum strategy to obtain the best precision in $r(0)$ for a given total number of measurements is to take twice as many measurements at the lower B field than at the higher field. We followed the alternate strategy of taking equal numbers of measurements at the two B-field values in order to improve the precision in dr/dB, and thereby obtain a better test for systematic errors.

The results for $r(0)$ and dr/dB grouped into three runs are summarized in Table VII. For comparison, the data at $F = 532.2$ V/cm are renormalized to the lower-field results, using the field correction of Sec. III B 1. It is satisfying that the $r(0)$ and dr/dB values are the same within experimental error for the three runs. Their grand average values are

$$r(0) = 1.015\,310\,9 \pm 0.000\,011\,6 \tag{56}$$

and

$$dr/dB = (28.60 \pm 0.48) \times 10^{-6} \text{ G}^{-1} . \tag{57}$$

The observed difference $\Delta r = r^+ - r^-$ for runs 1 and 2 at the two electric-field values are $\Delta r = (0.86 \pm 0.38) \times 10^{-4}$ and $\Delta r = (1.24 \pm 0.42) \times 10^{-4}$, in agreement with each other and with the expectation of Eq. (52). Run 3, obtained after remounting the photon collimator slits, gives a larger value of $\Delta r = (3.29 \pm 0.39) \times 10^{-4}$. All of the observed Δr have the expected order of magnitude, but the last one exceeds predictions by nearly two standard deviations. This may result from slight variations in the thickness of the thin Al films covering the exit slits of the photon collimators. Such variations would cause effective alignment errors that exceed the geometrical ones calculated from Eq. (52).

B. Systematic corrections

The above experimental value for the damping ratio includes the correction for a 1% background noise, but there remain further significant corrections. These include a correction for the finite pressure in the observation region, a correction for a small $2E1$ two-photon

TABLE VII. Observed damping ratios extrapolated to zero magnetic field, and their slopes at $F = 492.2$ V/cm and 532.2 V/cm.

Run	F (V/cm)	$r(0)$	$\frac{dr}{dB}$ (10^{-6} G^{-1})
1	492.2	1.015 3150(190)	28.48±0.64
2	492.2	1.015 2986(195)	29.10±0.67
3	532.2	1.015 3176(210)	
		1.015 3212(210)[a]	28.22±0.69[a]

[a]Same as run 3 renormalized from 532.2 to 492.2 V/cm.

component of the signal, a correction for averaging the signal over the finite solid angle of the detectors, and a correction for a relativistic angular shift. Another correction for beam bending in the field exists which is too small to affect the present results. Similarly, the small correction for the linear extrapolation of $r(B)$ to zero field resulting from the weak magnetic-field dependence of dr/dB of Eq. (50) can be neglected.

1. Pressure correction

Exchange of electrons between the spin-polarized ions in the beam and the residual gas along the 120-cm-long flight path from the spin polarizer to the observation region partially destroys the spin polarization and lowers the observed damping ratio. Under normal low-pressure (6×10^{-8} Torr) operating conditions, the principal component of the residual gas is N_2, which is introduced as a gas load by the gas cell for formation of the metastable He$^+$(2s) ions. To measure the correction, the pressure in the observation region was raised with N_2 gas to increase the noise level by a factor of 20. We now take the background noise, which is proportional to the pressure in the range 10^{-7}–10^{-5} Torr studied, as a measure of the true pressure. This pressure can no longer be determined with the ionization pressure gauge as it is located in the relatively strong operating magnetic fields of either 19 or 38 G, where it gives erroneous and magnetic-field-dependent readings.

For the quenching field $F = 492.2$ V/cm, high-pressure ($\sim 10^{-6}$ Torr) damping ratios were determined for the operating fields $B = 19.19$ and 38.41 G used in the main experiment. These two results were then used to extrapolate the low-pressure measurements to zero pressure. The resulting corrections for $B = 19.19$ and 38.41 G are $\delta r = (4.55 \pm 2.00) \times 10^{-6}$ and $(5.17 \pm 2.70) \times 10^{-6}$, respectively.

Since these corrections should in principle be independent of the magnetic field, we take their average $\delta R = (4.87 \pm 1.61) \times 10^{-6}$ as the pressure correction. The damping ratio of Eq. (56) corrected for noise then be-

comes $r = 1.0153158 \pm 0.0000117$, corresponding to an observed damping asymmetry at $F = 492.2$ V/cm of $A = (7.59970 \pm 0.00576) \times 10^{-3}$. This is the first entry in Table VIII.

2. Two-photon background

The quenching signal contains a small isotropic background from spontaneous $2E1$ decay of the $2\,{}^2S_{1/2}$ state. Since part of this background is added to the denominator $I(\pi/4) + I(3\pi/4)$ of Eq. (11), the A asymmetry is reduced. The correction factor can be conveniently expressed in the form

$$(\delta A / A_0)_{2E1} = \frac{\gamma(2s)}{\gamma(F)} \bar{\eta} \left[1 + \frac{R}{3} \right] , \qquad (58)$$

where $\gamma(2s) = 131.7$ s^{-1} is the $2E1$ decay rate [10–12],

$$\gamma(F) = \gamma(2p)(eF)^2 \left[\frac{|\langle 2s_{1/2}|z|2p_{1/2}\rangle|^2}{\mathcal{L}^2 + \Gamma^2/4} + \frac{|\langle 2s_{1/2}|z|2p_{3/2}\rangle|^2}{\mathcal{F}^2 + \Gamma^2/4} \right] \qquad (59)$$

is the field-induced decay rate [1], and $\bar{\eta}$ is the average efficiency for detecting $2E1$ photons relative to Ly-α radiation [3]. Using $\gamma(2s)/\gamma(F) = 3.455 \times 10^{-5}$ at $F = 492.2$ V/cm, the correction to the anisotropy is $\delta A = (0.00017 \pm 0.00002) \times 10^{-3}$ as listed in Table VIII.

3. Solid-angle correction

Since the apparatus averages the signal over the finite solid angle of observation, the observed asymmetry is too small. The fractional correction factor is similar to our earlier work [5] and is given by

$$(\delta A / A_{\text{obs}})_{\text{solid angle}}$$
$$= \frac{1}{2s^2} [p^2/2 + (1 - R)(\alpha^2/3 + \beta^2/4) + \beta^2/2] . \qquad (60)$$

TABLE VIII. Systematic corrections used to obtain the zeroth-order asymmetry A_0 and the lifetime from the measured value A_{exp}.

Quantity	Value
A_{exp}	$(7.59970 \pm 0.00576) \times 10^{-3}$
$(\delta A)_{2E1}$	$(0.00017 \pm 0.00002) \times 10^{-3}$
$(\delta A)_{\text{solid angle}}$	$(0.01023 \pm 0.00002) \times 10^{-3}$
$(\delta A)_{\text{rel angle}}$	$(0.00048 \pm 0.00000) \times 10^{-3}$
$A_2 F^2 + A_4 F^4$ [a]	$(0.01066) \times 10^{-3}$
$(\delta A)_{M2}$	$(0.00044) \times 10^{-3}$
$(\delta A)_{\text{rel}}$	$(0.00000) \times 10^{-3}$
$(\delta A)_{np}$	$-(0.00030) \times 10^{-3}$
A_0 (sum of above)	$(7.62138 \pm 0.00576) \times 10^{-3}$
$\gamma(2p_{1/2})$	$(1.002838 \pm 0.000756) \times 10^{10}$ rad/s
$\tau(2p_{1/2})$	$(0.99717 \pm 0.00075) \times 10^{-10}$ s

[a]Evaluated at $F = 492.2$ V/cm.

The parameters refer to the photon slit system of Fig. 4. The correction factor above ignores second-order corrections due to beam bending in the quenching field. Their relative importance for the damping asymmetry is much smaller than for the Lamb-shift anisotropy [3]. The correction factor of $(1.001\,346\pm0.000\,002)$ results in a solid-angle correction $\delta A = (0.010\,229\pm0.000\,016)\times10^{-3}$ as listed in Table VIII.

4. Relativistic angular shift

The intensities observed parallel to the observation axes of the photon detectors in the laboratory frame are emitted with an angular displacement of v/c in the comoving atomic frame. The net correction to the asymmetry is

$$(\delta A / A)_{\rm rel\,angle}=(1-R)(v/c)^2 . \tag{61}$$

The numerical value in Table VIII corresponds to our beam velocity $v=(2.543\pm0.010)\times10^8$ cm/s.

The sum of all the above corrections is used to reduce the observed asymmetry $A_{\rm exp}$ to an effective zero-order field-free value A_0 as shown in Table VIII. The level width $\Gamma(2p_{1/2})$, decay rate $\gamma=2\pi\Gamma$, and lifetime $\tau=\gamma^{-1}$ are then calculated from Eq. (17).

VII. DISCUSSION

The theoretical decay rate for the $2p_{1/2}$ state of a hydrogenic ion with nuclear charge Z and reduced mass $\mu=mM/(m+M)$ is

$$\gamma=4\pi cR_\infty(1-\mu/M)[1+(Z-1)\mu/M]^2$$
$$\times[1-2\ln(8/9)\alpha^2Z^2](2/3)^8\alpha^3Z^4 . \tag{62}$$

The correction factors are the reduced-mass correction, the nuclear-radiation correction, and the net relativistic correction arising from the transition-matrix element and transition frequency. The nuclear-radiation term takes into account that the nucleus as well as the electron is oscillating in the center-of-mass frame [12,13]. Not includ-

ed are QED corrections to the energies and interaction vertex. With the values of the fundamental constants $R_\infty=109\,737.315\,709(18)$ cm^{-1}, $\alpha^{-1}=137.035\,989\,5(61)$, and $\mu/M=1.370\,745\,62(3)\times10^{-4}$, the above gives a theoretical decay rate of $\gamma=1.003\,118\times10^{10}$ s^{-1} or $\tau=0.996\,891\times10^{-10}$ s.

The measured asymmetry corresponds to a lifetime τ of $(0.997\,17\pm0.000\,75)\times10^{-10}$ s in agreement with the above theoretical value. Our improved lifetime measurement is considerably more accurate than the beam-foil result of $(0.98\pm0.05)\times10^{-10}$ s by Lundin et al. [14] and our own previous measurement of $(0.9992\pm0.0026)\times10^{-10}$ s. It confirms basic radiation theory at the 0.075% level of accuracy for a fundamental one-electron atomic system. Thus the source of the discrepancy of several standard deviations between theory and experiment for the $\pm0.15\%$ lifetime measurements in neutral Li and Na [8,15] must lie either in the many-electron wave functions or in unsuspected experimental errors.

The agreement between the observed and predicted magnetic-field dependence of the damping ratio provides strong evidence that our result is free from systematic errors within the limits of the quoted precision. It is also satisfying that the observed and predicted difference in the damping ratios for $\hat{\mathbf{P}}=\pm\hat{\mathbf{v}}$ in Sec. VI A have the same magnitude, showing that the angular alignments of the detection system fall within the (effective) angular tolerance of $\sim3\times10^{-4}$ rad. Although deviations of this order significantly affect the measurement of the damping ratio, they only introduce an error in the measurement of the Lamb-shift anisotropy R no greater than 1 ppm. Hence our present measurement on the lifetime confirms the reliability of the anisotropy method used previously to measure the Lamb shift in He$^+$ [3].

ACKNOWLEDGMENTS

[1] G. W. F. Drake, in Spectrum of Atomic Hydrogen: Advances, edited by G. W. Series (World Scientific, Singapore, 1988).
[2] G. W. F. Drake and A. van Wijngaarden, in Physics of Higher-Ionized Atoms, edited by R. Marrus (Plenum, New York, 1989), pp. 159–166.
[3] A. van Wijngaarden, J. Kwela, and G. W. F. Drake, Phys. Rev. A 43, 3325 (1991).
[4] A. van Wijngaarden, R. Helbing, J. Patel, and G. W. F. Drake, Phys. Rev. A 25, 862 (1982).
[5] G. W. F. Drake, J. Patel, and A. van Wijngaarden, Phys. Rev. A 28, 3340 (1983).
[6] B. J. Miller, J. R. Fuhr, and G. A. Martin, in Bibliography on Atomic Transition Probabilities November 1977 through March 1980, Natl. Bur. Stand. (U.S.) Spec. Publ. No. 505 (U.S. GPO, Washington, DC, 1980); A. Weiss (private communication).
[7] Yu. L. Sokolov and V. P. Yakovlev, Zh. Eksp. Teor. Fiz. 83, 15 (1982) [Sov. Phys.—JETP 56, 7 (1982)]; V. G. Pal-

chikov, Yu. L. Sokolov, and V. P. Yakovlev, Pis'ma Zh. Eksp. Teor. Fiz. 38, 347 (1983); V. G. Palchikov, Yu. L. Sokolov, and V. P. Yakovlev, Metrologia 21, 99 (1985).
[8] A. Gaupp, P. Kuske, and H. J. Andrä, Phys. Rev. A 26, 3351 (1982).
[9] A. Dalgarno and J. T. Lewis, Proc. R. Soc. London, Ser. A 233, 70 (1956); A. Dalgarno and A. L. Stewart, ibid. 238, 269 (1956).
[10] G. W. F. Drake and R. B. Grimley, Phys. Rev. A 8, 157 (1973).
[11] S. P. Goldman and G. W. F. Drake, Phys. Rev. A 24, 183 (1981); F. A. Parpia and W. R. Johnson, ibid. 26, 1142 (1982).
[12] G. W. F. Drake, Phys. Rev. A 34, 2871 (1986).
[13] Z. Fried and A. D. Martin, Nuovo Cimento 29, 574 (1963); R. Bacher, Z. Phys. A 315, 135 (1984).
[14] L. Lundin, H. Ona, W. S. Bickel, and I. Martinson, Phys. Scr. 2, 213 (1970).
[15] A. Weiss, Can. J. Chem. (to be published).